Supplementary Materials

Iron Phosphide Precatalyst for Electrocatalytic Degradation of Rhodamine B Dye and Removal of *Escherichia coli* from Simulated Wastewater

Takwa Chouki [1], Manel Machreki [1], Jelena Topić [2], Lorena Butinar [3], Plamen Stefanov [4], Erika Jez [3], Jack S. Summers [5], Matjaz Valant [1], Aaron Fait [6] and Saim Emin [1, *]

[1] Materials Research Laboratory, University of Nova Gorica, Ajdovscina 5270, Slovenia

[2] Laboratory for Environmental and Life Sciences, University of Nova Gorica, Nova Gorica 5000, Slovenia

[3] Wine Research Centre, University of Nova Gorica, Glavni Trg 8, Vipava 5271, Slovenia

[4] Institute of General and Inorganic Chemistry, Bulgarian Academy of Sciences, Sofia 1113, Bulgaria

[5] Department of Chemistry and Physics, Western Carolina University, Cullowhee, North Carolina 28723, USA

[6] The Jacob Blaustein Institutes for Desert Research, Ben-Gurion University of the Negev, Midreshet Ben-Gurion, 84990, Israel

* Corresponding author: Saim Emin

Tel: +386 5 365 35 38; Fax: +386 5 3653 527; E-mail: saim.emin@ung.si

Text S1. Rietveld refinement analysis and Williamson–Hall method

The Rietveld refinement technique for powder-diffraction data is one of the whole pattern methods, used for crystal quantification [1], it's a multi-parameter curve fitting procedure [2]. The model function consists of a parameterized description of a curve that is fitted by least squares to the suite of data points that comprises the powder-diffraction scan [2]. This model function includes both the contributions from the sharp Bragg peaks from the crystalline component of the sample and the contribution from a smooth background that underlies the peaks [2]. The Rietveld refinement minimizes *R*, which is the sum of weighted and squared differences between observed and calculated intensities at each point in an XRD pattern. The procedure of minimizing *R* involves least squares refinement [1].

$$R = \sum_i W_i |y_i(\text{obs}) - y_i(\text{calc})|^2 \quad (1)$$

Where y_i (obs) and y_i (calc) are the observed and calculated intensities at point *i*, W_i is the weight assigned to each intensity. The result of a Rietveld refinement includes crystal structure information (lattice parameters, atomic coordinates, displacement factors, and site fractions) and macroscopic sample information (crystallite size, microstrain distribution, and crystalline phase fractions) [2]. There are many methods such as Williamsons Hall method, Warren–Averbach method etc., which considers the effect of the strain induced XRD peak broadening and can be used for the calculation of the intrinsic strain along with the crystallite size. Among these methods, Williamson–Hall (W–H) method found to be easy and simple. According to which, physical line broadening of XRD peak occurs due to the size and the intrinsic strain of the nanocrystals and the total broadening can be written as [3],

$$\beta_{\text{total}} = \beta_{\text{size}} + \beta_{\text{strain}} \quad (2)$$

In the present work, average cristallite size and intrinsic strain have been calculated using modified W–H equation [3],

$$\beta_{\text{hkl}} \times \cos(\theta) = \frac{k\lambda}{D} + 4\varepsilon \times \sin(\theta) \quad (3)$$

Where *D* is the crystallite size (nm), *k* is a constant (0.94), λ is the wavelength of the x-ray radiation (0.15406 nm), β is the full width at half maximum (FWHM) of the intense and broad peaks, ε is the intrinsic strain and θ is the Bragg's or diffraction angle [3]. This equation is an equation of a straight line and is known as the uniform deformation model (UDM) equation, which considers the isotropic nature of the crystals. Figure S1 shows the plotting of this equation, with the term (4Sinθ) along X-axis and (βCosθ) along Y-axis corresponding to each

diffraction peak for Fe_2P nanoparticles. This plotted straight line is a good fitted line, corresponding to all the values, as the correlation coefficient value of R^2 is 0.9284. The slope of this straight line provides the value of the intrinsic strain, whereas the intercept gives the average crystallite size of the Fe_2P nanocrystals [3].

The average crystallite size has been determined from the UDM approximately as 18 ± 0.0010 nm. Again, slope of the UDM plot has been found to be positive, which indicates the lattice expansion and hence produce an intrinsic strain in the nanocrystals [3]. From the slope, intrinsic strain has been calculated as 4.5×10^{-3} ± 0.0007 a.u.

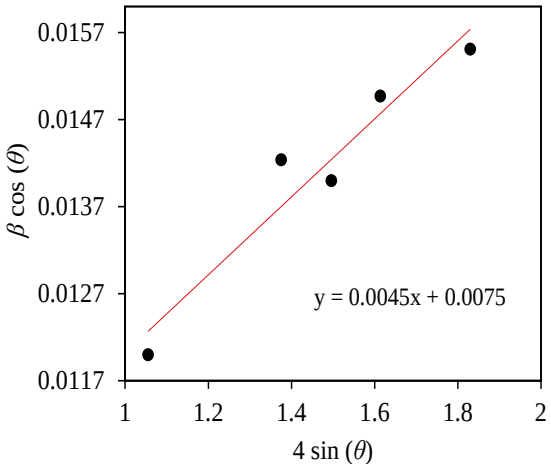

Figure S1. Williamson–Hall plot for the Fe_2P XRD pattern.

XRD pattern of Fe_2P after heat treatment

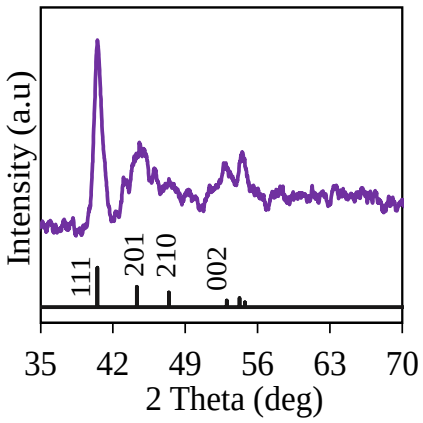

Figure S2. XRD pattern of Fe_2P after short heat treatment.

Size distribution of spheres

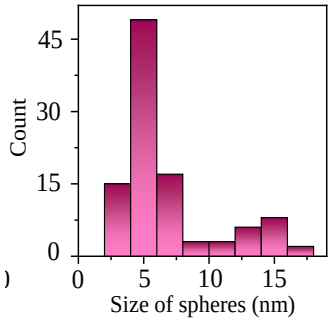

Figure S3. Size distribution of Fe_2P NSs.

Heat treatment procedure

To study the catalytic activity of the film before heat treatment, we conducted one LSV test for the obtained Fe_2P recorded at 5 mV s^{-1} in 10^{-5} M RhB + 0.06 M NaCl (pH 5). Before heat treatment, the current was too low.

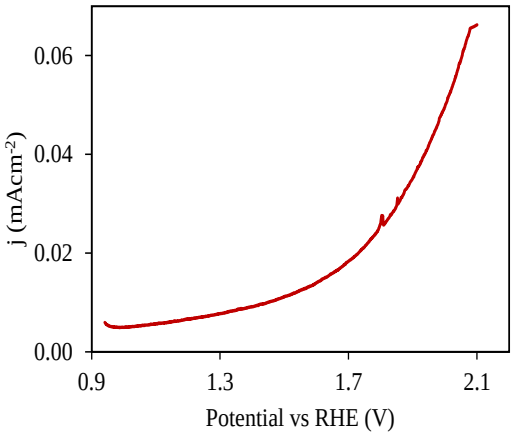

Figure S4. LSV characteristic of Fe_2P particles recorded in 10^{-5} M RhB + 0.06 M NaCl conducted before heat treatment.

Text S2. Tafel plots and electrochemical impedance spectroscopy

The pathway and kinetics of OER are generally investigated using semi-logarithmically plotted current-potential curve (Eq. 4), typically called a Tafel plot (Figure S5a).

$$\eta = a + b \cdot \log(j) \tag{4}$$

where j is the current density, a is the intercept and b is a coefficient, Tafel slope. Typical values of b for efficient water oxidation catalysts are in the range of 30 – 120 mV dec^{-1} [4].

When the values of *b* are high then these can be ascribed to different factors like (i) the observed reaction is limited by surface diffusion or some chemical steps is the rate determining step, (ii) mass transfer, (iii) the accumulation of oxygen bubbles or reactive oxygen species which block the active surface of the electrode, etc [5]. The determined values of *b* in this study are equal to 144 mV dec^{-1} (NaCl), 218 mV dec^{-1} (NH_4Cl), and 245 mV dec^{-1} (Na_2SO_4). Worth mentioning that in NaCl and NH_4Cl electrolytes the Tafel slope are not entirely from the OER reaction but involves competitive oxidation reaction of Cl^- ions (CER). For efficient catalysts like RuO_2 the Tafel slopes for CER are usually under 100 mV dec^{-1} [6]. Herein, the Tafel slopes of Fe_2P thin film reported in Cl^- electrolyte is ascribed both to OER and CER. Since, the Tafel slopes in Cl^- electrolyte is much lower it can be assumed that CER proceeds much efficiently than OER in the present system.

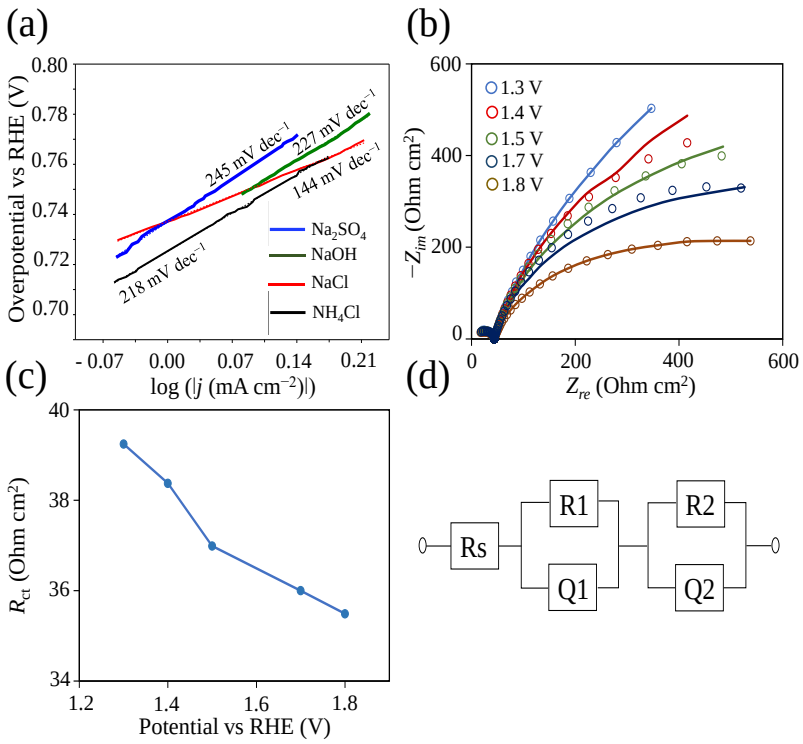

Figure S5. (a) Tafel plots of different electrolytes (0.06 M, pH 5) are given. (b) Nyquist plot of Fe_2P thin film in 0.06 M Na_2SO_4 (pH 5). (c) Charge transfer resistance (*R*2) versus applied voltages. (d) A circuit element used to fit the data shown in (b).

Text S3. Calculation of electrocatalytic active surface area

The CVs were measured in a non-Faradaic potential range (0.15−0.25 V vs RHE) at scan rates ranging from 20 to 100 mV s^{-1}. These results are shown in Figure S6. The double-layer capacitance (C_{DL}) of 0.023 mF was determined from the slope shown in Figure S6b and this

value was used to calculate ECSA using the expression ECSA = C_{DL}/C_s [7], where C_s = 40 μF cm^{-2} is the specific capacitance of flat film in 1 M KOH [8].

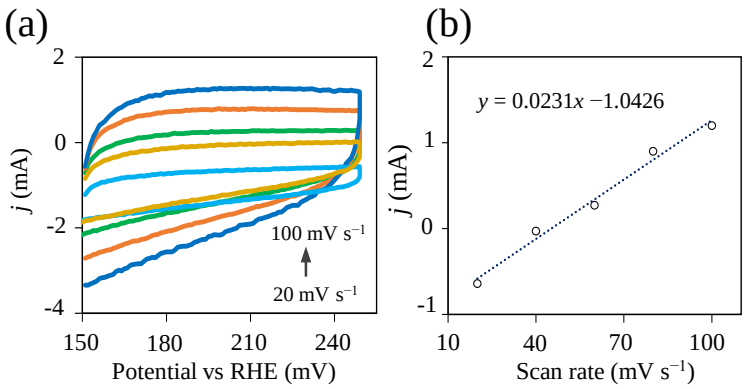

Figure S6. (a) CVs of Fe_2P at different scan rates in 1 M KOH. (b) Current vs scan rate taken from (a).

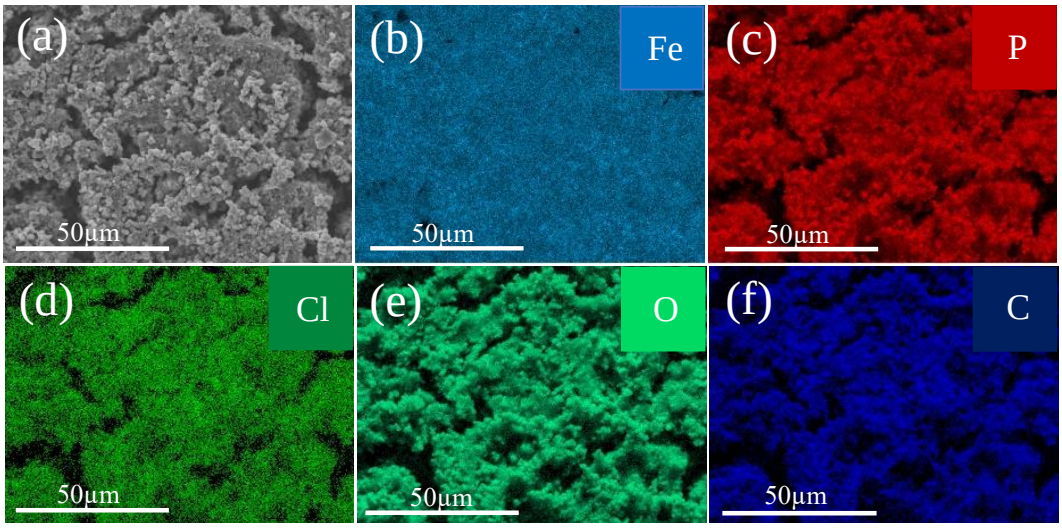

Figure S7. Images with elemental maps are given for Fe, P, Cl, O and C taken from the Fe_2P sample (after electrolysis) shown in image (a).

Time profiles of RhB degradation in 0.06 M NaCl conducted with Ti and Fe_2P–iron phosphate electrodes

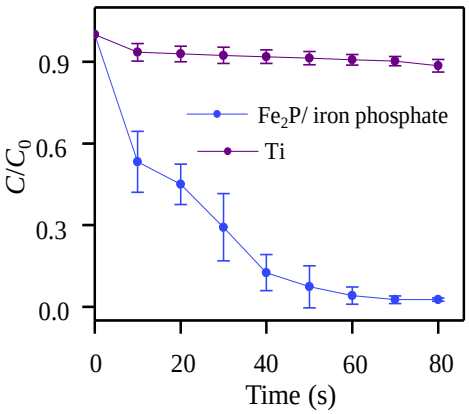

Figure S8. C/C_0 vs time in 0.06 M NaCl conducted with Ti and Fe_2P–iron phosphate electrodes at 2.0 V vs RHE.

Degradation efficiency of RhB

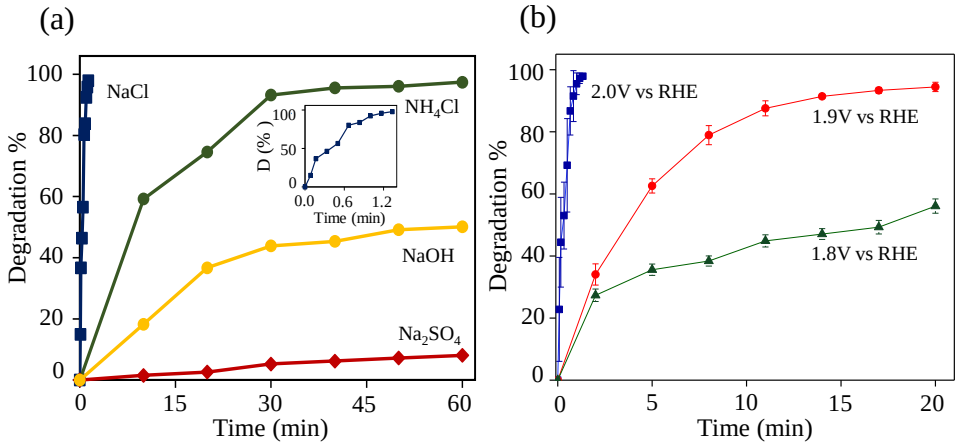

Figure S9. (a) Degradation efficiency in the presence of 0.06 M NaCl,0.06 M NH_4Cl, 0.06 M NaOH and 0.06 M Na_2SO_4 at 2.0 V vs RHE. The inset in (a) is a magnification of the degradation efficiency of NaCl. (b) Degradation efficiency of 0.06 M NaCl at different applied potentials.

Text S4. Kinetic models

The pseudo-second-order kinetic model was used to fit the experimental data using the following equation $1/C - 1/C_0 = k_2 t$, where C and C_0 are the concentrations of the dye at time t and time zero, and k_2 is a pseudo second-order rate constant calculated from the slope of the straight line [9].

Table S1. Pseudo first-order and pseudo-second order rate constants and correlation coefficients of RhB dye on Fe_2P–iron phosphate film.

	Pseudo-first order		Pseudo-second order	
	k_1 (min^{-1})	R^2	k_2 (M^{-1} min^{-1})	R^2
NaCl	2.6591	0.98	2.3105×10^6	0.74
NH_4Cl	0.0690	0.98	77348	0.93
Na_2SO_4	0.0015	0.99	76.8949	0.45
NaOH	0.0130	0.94	1696.4	0.91

Text S5. Fluorescence spectra of Fe_2P–iron phosphate catalyst in 20 µM coumarin

It is well-known that •OH radicals react with coumarin molecules to form highly fluorescent 7-hydroxycoumarin (7-HC) [10]. The EC experiment was carried out without RhB dye using 20 µM coumarin in 0.06 M NaCl. The concentration of 7-HC was recorded via a fluorescence spectrophotometer at an excitation wavelength of 332 nm. Calibration plot at different concentrations of 7-HC is presented in Figure S10a. The lack of emission peak from EC treated solutions confirm the absence of 7-HC (Figure S10b).

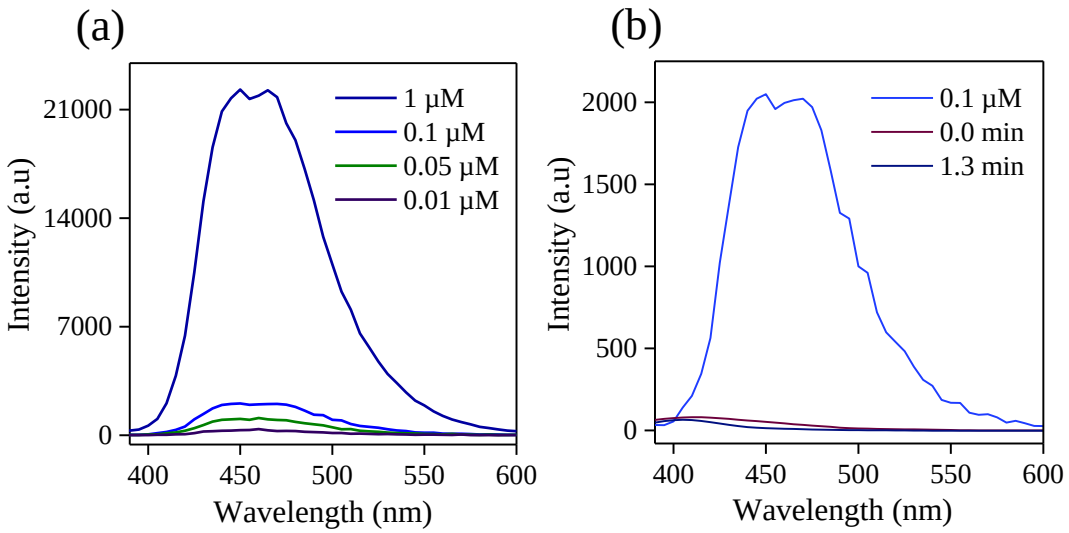

Figure S10. (a) The fluorescence emission spectra obtained (a) at different concentration of 7-HC and (b) before (0.0 min) and after (1.3 min) the electrochemical process with 20 µM coumarin as a probe molecule in 0.06 M NaCl. For comparison purpose in (b) is given also the intensity of 0.1 µM 7-HC standard.

Detection of HClO by DPD method

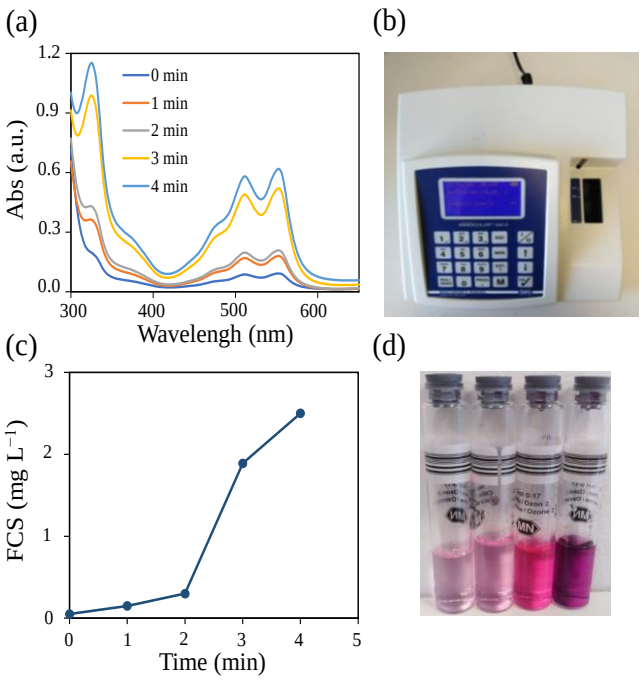

Figure S11. (a) Visible absorption spectra of the DPD–HClO solution. (b) Photometer Nanocolor 500 d used to measure the concentration of the produced HClO. (c) Formation of HClO (e.g., FCS) in 0.06 M NaCl solution (pH=5). (d) Change in color of the test kits containing the DPD reagent by adding the produced HClO.

The color of the test kits solution after adding the produced HClO gradually became deep.

MS measurement of H_2 and O_2 gas during the RhB degradation

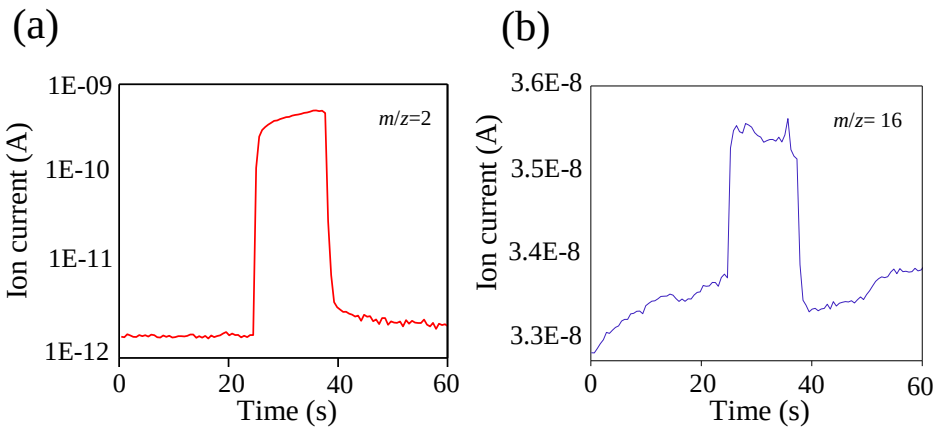

Figure S12. Ionic current vs time of (a) H_2, and (b) O_2 recorded using MS in 0.06 M NaCl and 10^{-5} M RhB solution under 2.0 V vs RHE.

Text S6. Degradation mechanism of RhB dye

Our results indicate that the degradation of RhB dye in Cl^- containing electrolyte is governed by RCS (Cl•, $Cl_2^{\bullet-}$, HClO, etc). The situation is different in Na_2SO_4 electrolyte where the dye degradation is caused by $SO_4^{\bullet-}$ and •OH. However, the degradation rate of RhB was slow in Na_2SO_4 and NaOH electrolytes which resulted respectively in only 8 % and ~ 50 % degradation efficiency after 60 min electrolysis (Figure S9). Therefore, the amount of formed $SO_4^{\bullet-}$ and •OH are negligible. Further, the experimental procedure carried out in coumarin (Figure S10) showed that the •OH radicals generation is blocked. Therefore, •OH radicals do not participate in dye degradation in the presence of Cl^- electrolyte. Oliveira et al. demonstrated that chlorine radicals (Cl• and $Cl_2^{\bullet-}$) are better oxidants than FCS (Cl_2, HClO, ClO^-) [11]. As reported by Cho et al. the formation of chlorine radicals occurs only at high anodic potentials >2.0 V vs NHE [12]. In our case the applied potential was maintained at 2.0 V vs RHE (e.g. 1.7 V vs NHE). Therefore, the formation of chlorine radicals (Cl• and $Cl_2^{\bullet-}$) is not favored during RhB degradation. The most probable reaction is the anodic oxidation of Cl^- ion to Cl_2 which occur at relatively low potentials (E° = 1.36 V vs NHE) [13]. At pH 5 dissolved Cl_2 appear mainly in the form of HClO (Eqs. (6) – (7)) [14].

$$2Cl^- \rightarrow Cl_{2\,(aq)} + 2e^- \quad (6)$$

$$Cl_2 + H_2O \leftrightarrow HClO + H^+ + Cl^- \quad (7)$$

It is well-known that HClO is a strong oxidizing agent which can degrade organic molecules [15]. Therefore, in-situ generated HClO plays an essential role in RhB degradation.

Text S7. Calculation of the current generation efficiency of HClO

The current generation efficiency of HClO, (η_{HClO} (%)) was calculated using the following equation: η_{HClO} (%) = ([HClO] × V/(I×t/2F) × 52460) × 100 (%), where F is the Faraday constant (96485 C mol^{-1}), V is the electrolyte volume (0.25 L), I is the current (A), t is the reaction time (s). and 52460 is the molecular weight of hypoclorous acid (mg mol^{-1}). Under potentiostatic conditions (at 2.0 V vs RHE) during 4 min reaction time in 0.06 M NaCl, the η_{HClO} was calculated as 73.7 % [16].

LSV plots and SEM images of Fe_2P–iron phosphate electrode recorded before and after the recycling test

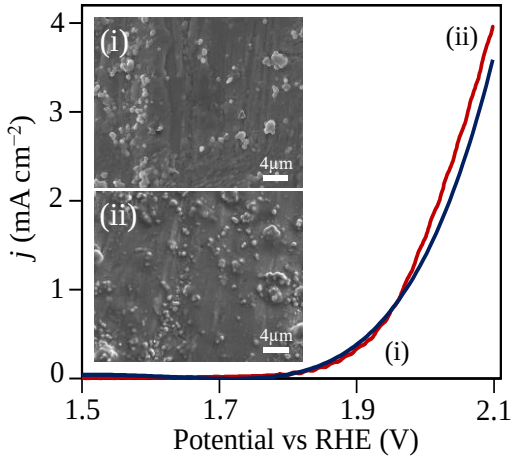

Figure S13. LSV plots and SEM images (insets) of Fe_2P–iron phosphate films recorded before (i) and after (ii) the recycling test.

HPLC in the presence of different electrolytes

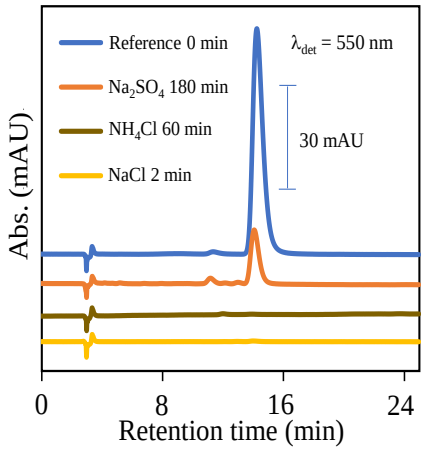

Figure S14. HPLC of 1×10^{-5} M RhB solution in the presence of NaCl, NH_4Cl and Na_2SO_4.

Text S8. Phytotoxicity test using *Lepidium sativum* L

L. sativum was used to assess the acute toxicity of RhB before and after treatment in 0.06 M NaCl pH 5. RhB model solutions were prepared and degraded as described in EC section . In the experiment 15 seeds of *L. sativum* were evenly palced on a filter paper in Petri dish (Ø90 mm) and exposed by adding 3 ml of treated and untreated RhB model solution (sample RhB

after and RhB before, respectively). Control (C) was also included by adding distilled water to the seeds. Incubation was performed at room temperature and after 72 h seed germination and root growth were evaluated. Experiment was done in triplicate for each treatment. Relative germination percentage (RGP), relative radicle growth (RRG), germination index (GI), seed germination number (SGN) and average root length (ARL) were calculated according to the methodology described [17]. Seed germination and root growth of *L. sativum* was used to evaluate the phytotoxic effect of tested RhB dye solutions in 0.06 M NaCl pH 5. Inhibition (%) values are 20.5 and 16 % for untreated and EC treated RhB solutions, respectively (Eq. 8). The descend in the inhibition value shows that the toxicity of RhB was sligtly decreased for the treated RhB solution. Other useful parameters evaluated for the untreated and EC treated RhB solutions are the RGP (%): 95 (before)/ 100 (after); RRG (%): 79.5 (before)/84.0 (after); and GI (%): 75.9 (before)/ 84.0 (after); SGN: 14 (before)/ 15 (after) and ARL: 17.7 (before)/ 18.9 (after). The treated water gives higher values for all parameters which is considered beneficial for the plants growth.

Inhibition (%) was calculated as follow:

$$\text{Inhibition (\%)} = [(\text{Root length (C)} - \text{Root length (sample)})/\text{Root length (C)}] \times 100 \quad (8)$$

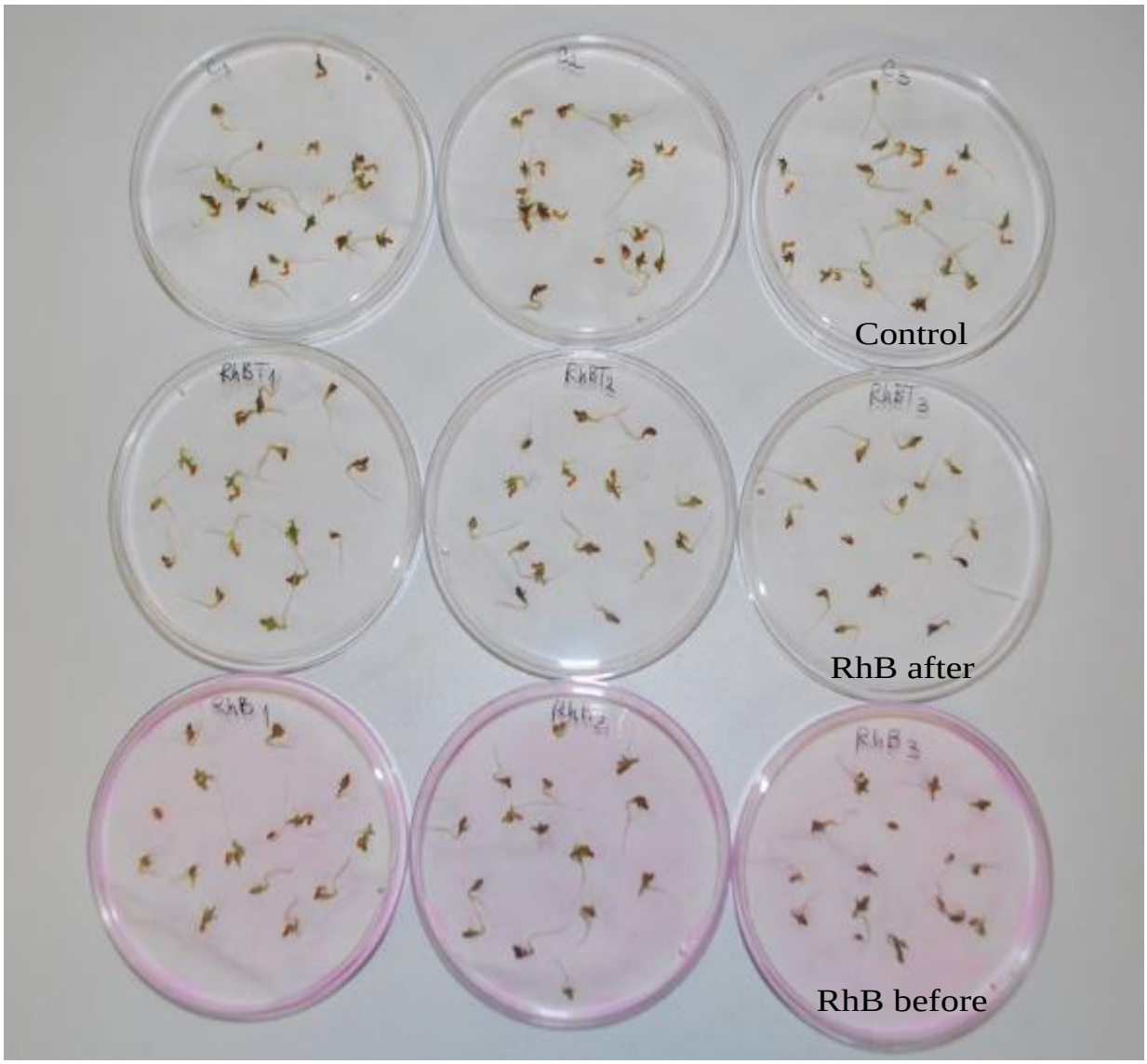

Figure S15. Images of *Lepidium sativum* L. incubated in Petri dishes with RhB before and after EC treatment.

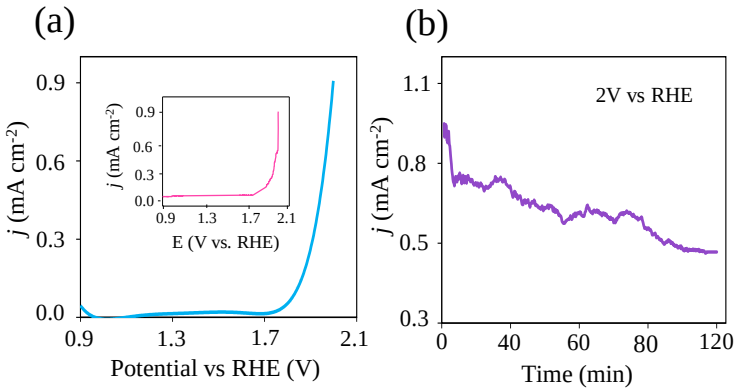

Figure S16. (a) LSV of Fe_2P–iron phosphate catalyst in 0.06 M NaCl seeded with 1.1×10^8 CFU/ml of *E. coli* bacteria at pH 5. (b) *I–t* plot obtained in 0.06 M NaCl + 1.1×10^8 CFU/ml of *E. coli* (pH 5) at 2.0 V vs RHE.

Table S2. Selected materials used in EC degradation of different dye molecules.

Material	Dye	Electrolyte	C_0 (mg/L)	Electrolysis time (min)	Removal (%)	Ref.
PbO_2	BR19	Na_2SO_4	25	120	100	[18]
Ti/Sb_2O_5-SnO_2	RR120	Na_2SO_4	1500	375	95	[19]
ACF	AR27	Na_2SO_4	80	480	99	[20]
Graphite	VB1	–	200	30	14	[21]
BDD	DR80	Na_2SO_4	350	1440	99	[22]
BDD	DY3	NaCl	100	50	>90	[23]
Ti/BDD	RD15	Na_2SO_4	1000	120–240	>95	[24]
NB/BDD	BR19	Na_2SO_4	25	18	95	[18]
TiO_2	AR27	Na_2SO_4	25	100	94	[25]
V/TiO_2	AR27	Na_2SO_4	25	40	99	[25]
Ti/Pt	BR13	NaCl	100	–	99.9	[26]
Graphite	RV2	NaCl	100	60	95	[27]
Fe Rod	MB	Na_2SO_4	10	60	86.46	[28]
Fe_2P–iron phosphate	**RhB**	**NaCl**	**4.8**	**1.3**	**98**	**Present study**
Fe_2P–iron phosphate	**RhB**	**NH_4Cl**	**4.8**	**60**	**97**	**Present study**

Table S3. Selected materials used in EC inactivation of E.coli bacteria.

Material	Electrolyte	Electrolysis time (min)	Applied current ($mA\ cm^{-2}$)	Removal (%)	Ref.
Pt	0.2 M KH_2PO_4	180	100	~ 90	[29]
Ti/TiO_2-RuO_2	0.01 M Na_2SO_4-0.1 M $NaNO_3$	0.55	> 30	insignificant	[30]

BDD	0.2 M KH_2PO_4	120	33	≤ 99.9	[31]
TiO_2	1.5 mM buffered NaCl solution	20	0.66 to 2.63	99.99	[32]
BDD	0.2 M Na_2SO_4	120	5	99.68	[33]
DSA	0.08 M Na_2SO_4	60	75	98.9	[34]
Fe_2P–iron phosphate	**0.06 M NaCl**	**40**	**0.9**	**100**	**Present study**

Text S9. Synthesis and characterization of Fe_2P thin film

We carried out the synthesis of Fe_2P NPs under Ar atmosphere at 300 °C. Typical procedure includes the addition of 10 ml OLA, 1.0 ml SQ and 3.14 g TPP into a three-neck flask (100 ml). We heated the mixture to 150 °C (heating rate: 10 °C min^{-1}). Once the TPP dissolves 0.6 g $Fe(CO)_5$ was rapidly injected into the flask. Later, the temperature was gradually rised and held at 300 °C for 15 min. After cooling down the suspension to 60 °C, we isolated the Fe_2P NPs by adding ethanol and acetone (v/v 1:1) followed by centrifugation at 7000 rpm for 10 min. The Fe_2P NPs were isolated as a solid material after decantation and drying at 50 ºC. We dispersed the obtained powder (0.3 g) in 3 ml $CHCl_3$ and spin-coated it on Ti plates at 1000 rpm for 15 s. The obtained Fe_2P films were heat treated in a tube furnace at 450 °C under Ar gas (99.999 % Messer) for 30 min (heating rate: 8 °C min^{-1}). Short heat treatment was performed to activate the Fe_2P catalyst by organic ligands removal and to improve the catalyst adhesion onto the substrate [35].

The morphology of Fe_2P film was studied using a SEM (JEOL JSM 7100 F) equipped with a field-emission electron gun and coupled to an energy dispersive X-ray spectrometer (EDS) (Oxford Instruments, X-Max^N), High resolution (HR) TEM studies were carried out with JEOL 2100F operating at 200 kV. XRD data were recorded using MiniFlex 600 W (Rigaku) diffractometer with Cu-K_α radiation. Phase identification was performed with the PDXL software using the crystallography open database. Rietveld analysis of Fe_2P thin film was carried out using the MAUD software [36]. XPS measurements were carried out using an AXIS

Supra electron spectrometer (Kratos Analytical Ltd., Manchester, UK), using Al-Kα radiation with photon energy of 1486.6 eV. Electrochemical measurements were done in a three-electrode system with a Cappuccino cell. An O-ring was used to define the electrode area to 0.283 cm^2. The potential of the working electrode was controlled by a potentiostat (EDAQ SP1). A graphite plate and a Ag/AgCl (Sigma-Aldrich) were used as the counter and reference electrodes, respectively. Experimentally measured potentials were converted to the reversible hydrogen electrode (RHE) scale using the Nernst equation: $E_{RHE} = E_{Ag/AgCl} + E^o_{Ag/AgCl} + 0.059\times pH$. In this equation, $E_{Ag/AgCl}$ was the measured potential against the Ag/AgCl reference electrode and $E^o_{Ag/AgCl}$ was taken as 0.197 V at 25 °C. The electrochemical impedance spectroscopy (EIS) of Fe_2P thin films were studied in 0.06 M Na_2SO_4 solution at various potentials from 1.3 to 1.8 V vs RHE. The applied frequency ranged from 100 mHz to 1 MHz with an amplitude of 10 mV. The measured EIS data was fitted using the Zview software. To determine the effective electrochemical active surface area (ECSA), cycling voltammetries (CVs) were measured in a non-Faradaic potential range from 0.15 to 0.25 V vs RHE in 1 M KOH at different scan rates (20−100 mV s^{-1}) and the measured potentials were converted to RHE scale using the Nernst equation: $E_{RHE} = E_{Hg/HgO} + E^o_{Hg/HgO} + 0.059\times pH$ where $E^o_{Hg/HgO}$ was taken as 0.098 V at 25 °C

Text S10. Catalyst evaluation

The degradation of RhB was conducted in a two-compartment cell comprising anodic (80 mL) and cathodic (55 mL) chambers separated by a proton exchange membrane (Nafion-115) (Figure S17). All the experiments were performed at 25 ºC using Fe_2P thin film as a working electrode (area 9 cm^2), Ag/AgCl electrode as the reference electrode, and a graphite plate as the counter electrode. The counter and working electrodes are kept 3 cm apart. For comparison, commercial Ti plate was used as working electrode. Initial dye solutions contained 1×10^{-5} M RhB and 0.06 M electrolytes (NH_4Cl, NaCl or Na_2SO_4) at pH 5. General characteristics of RhB are given in Table S4. The degradation of RhB dye at different reaction times was monitored with a Perkin Elmer Lambda 25 UV-VIS spectrophotometer. The concentration of free chlorine species mainly as HClO was estimated by measuring the absorbance at 515 nm of N,N-diethyl-p-phenylenediamine (DPD) colorimetric test kits (tube test Nanocolor chlorine/ozone 2, REF 985017) [16] with a UV-VIS spectrophotometer (Macherey Nagel, Nanocolor 500d) for a concentration range of 0.0 to 2.5 $mg\cdot L^{-1}$. Analysis of collected gases during the decomposition process was achieved using mass spectrometry (MS-Pfieffer Vacuum ThermoStar). The HPLC analyses were carried out on an Agilent

Technologies 1100 equipped with a quaternary pump, autosampler and diode array detector (Agilent Technologies, Palo Alto, California, USA). Mobile phase of methanol water in the ratio 60/40 was used in isocratic mode at 1 mL min^{-1} flow rate for 25 min. Separation was carried out on Kromasil C18 column (150 x 4.6 mm, 5 µm i.d.) (Sigma-Aldrich, Darmstadt, Germany) with the column temperature set at 30 °C. We injected 40 µL of sample into the HPLC column. Different detection wavelengths (λ_{det}) from 200 to 550 nm were used in this study. Formation of •OH radicals was studied using photoluminescence measurements (FL920 spectrophotometer, Edinburgh Instruments) with coumarin.

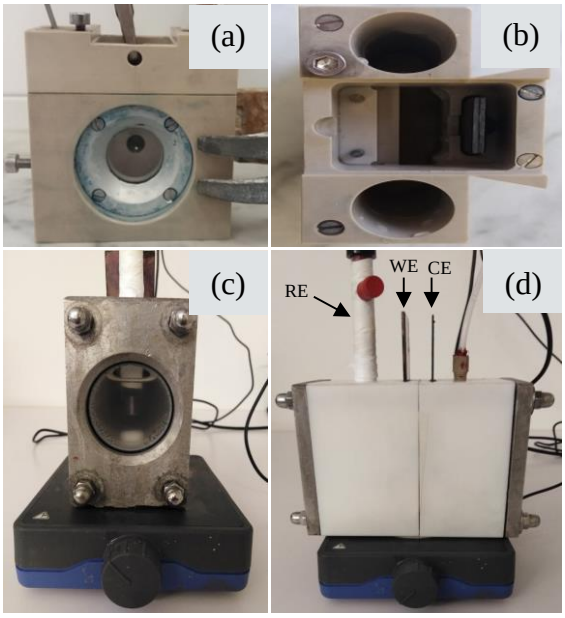

Figure S17. Photograph of the cappuccino cell used to record the LSV, CV and EIS and measurements in (a) side-view and (b) top-view. The cell used in the dye degradation studies: (c) side-view and (d) complete view.

Table S4. Characteristics of RhB dye.

Formula	**$C_{28}H_{31}ClN_2O_3$**
Class	Triphenylmethane
CAS	81-88-9
Molecular mass (g mol^{-1})	479.02
Solubility in water (g L^{-1}, 20 °C)	8 to 15
λmax (nm)	550

Chemical structure of RhB dye

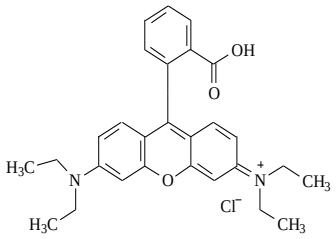

References

1. Zhou, X.; Liu, D.; Bu, H.; Deng, L.; Liu, H.; Yuan, P.; Du, P.; Song, H. XRD-based quantitative analysis of clay minerals using reference intensity ratios, mineral intensity factors, Rietveld, and full pattern summation methods: A critical review. *Solid Earth Sci.* **2018**, *3*, 16–29. https://doi.org/10.1016/j.sesci.2017.12.002.

2. Von Dreele, R.B. Protein crystal structure analysis from high-resolution X-Ray powder-diffraction data. *Methods Enzymol.* **2003**, *368*, 254–267. https://doi.org/10.1016/S0076-6879(03)68014-6.

3. Nath, D.; Singh, F.; Das, R. X-ray diffraction analysis by Williamson-Hall, Halder-Wagner and size-strain plot methods of CdSe nanoparticles- a comparative study. *Mater. Chem. Phys.* **2020**, *239*, 122021. https://doi.org/10.1016/j.matchemphys.2019.122021.

4. Zhu, K.; Ren, X.; Sun, X.; Zhu, L.; Sun, Z. Effect of supporting electrolyte on the surface corrosion and anodic oxidation performance of graphite electrode. *Electrocatalysis* **2019**, *10*, 549–559. https://doi.org/10.1007/s12678-019-00541-6.

5. Society, T.E. Water electrolysis using diamond thin film electrodes. *J. Electrochem. Soc.* **1998**, *145*, 2358.

6. Kuo, D.Y.; Paik, H.; Nelson, J.N.; Shen, K.M.; Schlom, D.G.; Suntivich, J. Chlorine evolution reaction electrocatalysis on RuO_2(110) and IrO_2(110) grown using molecular-beam epitaxy. *J. Chem. Phys.* **2019**, *150*, 041726. https://doi.org/10.1063/1.5051429.

7. Chouki, T.; Donkova, B.; Aktarla, B.; Stefanov, P.; Emin, S. Growth of $MoSe_2$ electrocatalyst from metallic molybdenum nanoparticles for efficient hydrogen evolution. *Mater. Today Commun.* **2021**, *26*, 101976. https://doi.org/10.1016/j.mtcomm.2020.101976.

8. McCrory, C.C.L.; Jung, S.; Peters, J.C.; Jaramillo, T.F. Benchmarking heterogeneous electrocatalysts for the oxygen evolution reaction. *J. Am. Chem. Soc.* **2013**, *135*, 16977–16987. https://doi.org/10.1021/ja407115p.

9. Sivarajasekar, N.; Srileka, S.; Samson Arun Prasath, S.; Robinson, S.; Saravanan, K. Kinetic

modeling for biosorption of Metylene Blue onto H_3PO_4 activated acacia arabica. *Carbon Lett.* **2008**, *9*, 181–187. https://doi.org/10.5714/cl.2008.9.3.181.

10. Mehta, A.; Mishra, A.; Kainth, S.; Basu, S. Carbon quantum dots/TiO_2 nanocomposite for sensing of toxic metals and photodetoxification of dyes with kill waste by waste concept. *Mater. Des.* **2018**, *155*, 485–493. https://doi.org/10.1016/j.matdes.2018.06.015.

11. Oliveira, F.H.; Osugi, M.E.; Paschoal, F.M.M.; Profeti, D.; Olivi, P.; Zanoni, M.V.B. Electrochemical oxidation of an acid dye by active chlorine generated using Ti/$Sn_{(1-x)}Ir_xO_2$ electrodes. *J. Appl. Electrochem.* **2007**, *37*, 583–592. https://doi.org/10.1007/s10800-006-9289 6.

12. Cho, K.; Hoffmann, M.R. Urea degradation by electrochemically generated reactive chlorine species: Products and reaction pathways. *Environ. Sci. Technol.* **2014**, *48*, 11504–11511. https://doi.org/10.1021/es5025405.

13. Kusmierek, E. Semiconductor electrode materials applied in photoelectrocatalytic wastewater treatment—An overview. *Catalysts* **2020**, *10*, 1–49. https://doi.org/10.3390/catal10040439.

14. Baddouh, A.; Bessegato, G.G.; Rguiti, M.M.; El Ibrahimi, B.; Bazzi, L.; Hilali, M.; Zanoni, M.V.B. Electrochemical decolorization of Rhodamine B dye: Influence of anode material, chloride concentration and current density. *J. Environ. Chem. Eng.* **2018**, *6*, 2041–2047. https://doi.org/10.1016/j.jece.2018.03.007.

15. Kothari, M.S.; Shah, K.A. Electrochemical oxidation for decolorization of Rhodamine-B dye using mixed metal oxide electrode: Modeling and optimization. *Water Sci. Technol.* **2020**, *81*, 720–731. https://doi.org/10.2166/wst.2020.151.

16. Koo, M.S.; Chen, X.; Cho, K.; An, T.; Choi, W.; Chen, X.; Cho, K.; An, T.; Choi, W. In situ photoelectrochemical chloride activation using a WO_3 electrode for oxidative treatment with simultaneous H_2 evolution under visible light. *Environ. Sci. Technol.* **2019**, *53*, 9926–9936. https://doi.org/10.1021/acs.est.9b02401.

17. Mañas, P.; De las Heras, J. Phytotoxicity test applied to sewage sludge using Lactuca sativa L. and Lepidium sativum L. seeds. *Int. J. Environ. Sci. Technol.* **2018**, *15*, 273–280. https://doi.org/10.1007/s13762-017-1386-z.

18. Andrade, L.S.; Ruotolo, L.A.M.; Rocha-Filho, R.C.; Bocchi, N.; Biaggio, S.R.; Iniesta, J.; García-Garcia, V.; Montiel, V. On the performance of Fe and Fe,F doped Ti-Pt/PbO_2 electrodes in the electrooxidation of the Blue Reactive 19 dye in simulated textile wastewater. *Chemosphere* **2007**, *66*, 2035–2043. https://doi.org/10.1016/j.chemosphere.2006.10.028.

19. Chen, X.; Chen, G.; Gao, F.; Yue, P.L. High-performance Ti/BDD electrodes for pollutant oxidation. *Environ. Sci. Technol.* **2003**, *37*, 5021–5026. https://doi.org/10.1021/es026443f.

20. Fan, L.; Zhou, Y.; Yang, W.; Chen, G.; Yang, F. Electrochemical degradation of Amaranth aqueous solution on ACF. *J. Hazard. Mater.* **2006**, *137*, 1182–1188. https://doi.org/10.1016/j.jhazmat.2006.04.008.

21. Cameselle, C.; Pazos, M.; Sanromán, M.A. Selection of an electrolyte to enhance the electrochemical decolourisation of indigo. Optimisation and scale-up. *Chemosphere* **2005**, *60*, 1080–1086. https://doi.org/10.1016/j.chemosphere.2005.01.018.

22. Lopes, A.; Martins, S.; Morão, A.; Magrinho, M.; Gonçalves, I. Degradation of a textile dye C. I. Direct Red 80 by electrochemical processes. *Port. Electrochim. Acta* **2004**, *22*, 279–294. https://doi.org/10.4152/pea.200403279.

23. Salazar, R.; Ureta-Zañartu, M.S.; González-Vargas, C.; Brito, C. do N.; Martinez-Huitle, C.A. Electrochemical degradation of industrial textile dye disperse yellow 3: Role of electrocatalytic material and experimental conditions on the catalytic production of oxidants and oxidation pathway. *Chemosphere* **2018**, *198*, 21–29. https://doi.org/10.1016/j.chemosphere.2017.12.092.

24. Chen, X.; Gao, F.; Chen, G. Comparison of Ti/BDD and Ti/SnO_2-Sb_2O_5 electrodes for pollutant oxidation. *J. Appl. Electrochem.* **2005**, *35*, 185–191. https://doi.org/10.1007/s10800-004-6068-0.

25. Chang, J.H.; Wang, Y.L.; Dong, C. Di; Shen, S.Y. Electrocatalytic degradation of azo dye by vanadium-doped TiO_2 nanocatalyst. *Catalysts* **2020**, *10*, 1–14. https://doi.org/10.3390/catal10050482.

26. Ozturk, D.; Yilmaz, A.E. Investigation of electrochemical degradation of Basic Red 13 dye in aqueous solutions based on COD removal: Numerical optimization approach. *Int. J. Environ. Sci. Technol.* **2020**, *17*, 3099–3110. https://doi.org/10.1007/s13762-020-02692-2.

27. Hamad, H.; Bassyouni, D.; El-Ashtoukhy, E.S.; Amin, N.; Abd El-Latif, M. Electrocatalytic degradation and minimization of specific energy consumption of synthetic azo dye from wastewater by anodic oxidation process with an emphasis on enhancing economic efficiency and reaction mechanism. *Ecotoxicol. Environ. Saf.* **2018**, *148*, 501–512. https://doi.org/10.1016/j.ecoenv.2017.10.061.

28. Teng, X.; Li, J.; Wang, Z.; Wei, Z.; Chen, C.; Du, K.; Zhao, C.; Yang, G.; Li, Y. Performance and mechanism of methylene blue degradation by an electrochemical process. *RSC Adv.* **2020**, *10*, 24712–24720. https://doi.org/10.1039/d0ra03963b.

29. Jeong, J.; Kim, J.Y.; Cho, M.; Choi, W.; Yoon, J. Inactivation of Escherichia coli in the

electrochemical disinfection process using a Pt anode. *Chemosphere* **2007**, *67*, 652–659. https://doi.org/10.1016/j.chemosphere.2006.11.035.

30. Li, X.Y.; Diao, H.F.; Fan, F.X.J.; Gu, J.D.; Ding, F.; Tong, A.S.F. Electrochemical wastewater disinfection: Identification of its principal germicidal actions. *J. Environ. Eng.* **2004**, *130*, 1217–1221. https://doi.org/10.1061/(asce)0733-9372(2004)130:10(1217).

31. Jeong, J.; Kim, J.Y.; Yoon, J. The role of reactive oxygen species in the electrochemical inactivation of microorganisms. *Environ. Sci. Technol.* **2006**, *40*, 6117–6122. https://doi.org/10.1021/es0604313.

32. Ahmadi, A.; Wu, T. Inactivation of E. coli using a novel TiO_2 nanotube electrode. *Environ. Sci. Water Res. Technol.* **2017**, *3*, 534–545. https://doi.org/10.1039/c6ew00319b.

33. Li, H.; Zhu, X.; Ni, J. Inactivation of Escherichia coli in Na_2SO_4 electrolyte using boron-doped diamond anode. *Electrochim. Acta* **2010**, *56*, 448–453. https://doi.org/10.1016/j.electacta.2010.08.055.

34. Gusmão, I.C.C.P.; Moraes, P.B.; Bidoia, E.D. Studies on the electrochemical disinfection of water containing Escherichia coli using a dimensionally stable anode. *Brazilian Arch. Biol. Technol.* **2010**, *53*, 1235–1244. https://doi.org/10.1590/s1516-89132010000500029.

35. Chouki, T.; Machreki, M.; Emin, S. Solvothermal synthesis of iron phosphides and their application for efficient electrocatalytic hydrogen evolution. *Int. J. Hydrogen Energy* **2020**, *45*, 21473–21482. https://doi.org/10.1016/j.ijhydene.2020.05.257.

36. Rasras, A.; Hamdi, R.; Mansour, S.; Samara, A.; Haik, Y. Study of the magnetocaloric effect in single-phase antiferromagnetic $GdMnO_3$. *J. Phys. Chem. Solids* **2021**, *149*, 109798. https://doi.org/10.1016/j.jpcs.2020.109798.